Commun Nonlinear Sci Numer Simulat 104 (2022) 106016

Contents lists available at ScienceDirect

Commun Nonlinear Sci Numer Simulat

journal homepage: www.elsevier.com/locate/cnsns

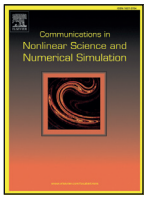

A bridge between invariant dynamical structures and uncertainty quantification

G. García-Sánchez [a], A.M. Mancho [a,*], S. Wiggins [b]

[a] Instituto de Ciencias Matemáticas, CSIC, C/Nicolás Cabrera 15, Campus Cantoblanco, Madrid 28049, Spain
[b] School of Mathematics, Fry Building, Woodland Road, University of Bristol, Bristol BS8 1UG, United Kingdom

ARTICLE INFO

Article history:
Available online 10 September 2021

Keywords:
Uncertainty quantification
Dynamical systems
Ocean data sets
Oil spill

ABSTRACT

We develop a new quantifier for forward time uncertainty for trajectories that are solutions of models generated from data sets. Our uncertainty quantifier is defined on the phase space in which the trajectories evolve and we show that it has a rich structure that is directly related to phase space structures from dynamical systems theory, such as hyperbolic trajectories and their stable and unstable manifolds. We apply our approach to an ocean data set, as well as standard benchmark models from deterministic dynamical systems theory. A significant application of our results, is that they allow a quantitative comparison of the transport performance described from different ocean data sets. This is particularly interesting nowadays when a wide variety of sources are available since our methodology provides avenues for assessing the effective use of these data sets in a variety of situations.

1. Introduction

Uncertainty Quantification (UQ) searches for a quantitative characterization of uncertainties in computational models of real-world applications. Uncertainties associated to these models have been studied for many years. Depending on the context uncertainties can arise as a result of noisy or incomplete data, errors introduced by numerical models, or by the lack of complete understanding of the governing physical processes. This work deals with uncertainty related to deterministic models, which occurs due to unknown aspects of the model, and not with that uncertainty derived from the presence of stochastic or noisy processes. A comparison between these two types of uncertainty may be found in Frenklach et al. [1].

In geophysical contexts uncertainty is a topic of much interest because it is inherent to the equations describing the motion of fluids, such as the ocean or the atmosphere. The motivation of this paper is to acquire a deeper understanding of uncertainty quantification that allows a better characterization of its presence in ocean models. Large amount of oceanic data are now becoming available. For example, the Copernicus Marine Environment Monitoring Service (CMEMS) provides regular and systematic information about the physical state and dynamics of the ocean for the global ocean and the European regional seas. The data cover the current and future state of variables and the provision of retrospective data records (re-analysis). Other oceanic services include ocean currents supplied by altimeter satellites, such as AVISO; the HY-

* Corresponding author.
E-mail address: a.m.mancho@icmat.es (A.M. Mancho).

https://doi.org/10.1016/j.cnsns.2021.106016

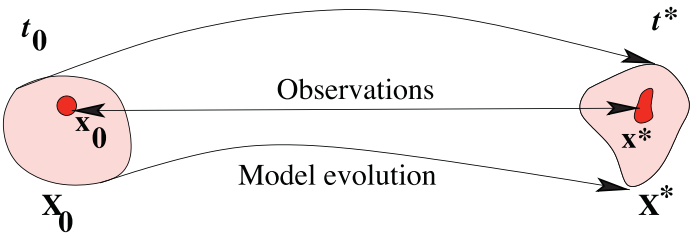

Fig. 1. A graphical representation of two sequential observations and their evolution according to a mathematical model. The initial observation at time t_0 is expressed by the red initial condition $\mathbf{x_0}$. The final observed state $\mathbf{x}^*$ at time t^* is referred to as the "target". The evolution law for these observations is unknown, but is approximated by a model, which in our setting involves the velocities $\mathbf{v}(\mathbf{x}, t)$ of the system (1). The evolution according to a model of a neighbourhood of points, $\mathbf{X_0}$, close to the initial observation, $\mathbf{x_0}$, is illustrated with the pink colour.

brid Coordinate Ocean Model (HYCOM), a consortium, which is a multi-institutional effort, sponsored by the National Ocean Partnership Program (NOPP), as part of the U. S. Global Ocean Data Assimilation Experiment (GODAE), to develop and evaluate a data-assimilative hybrid coordinate ocean models, etc. Validating data outputs from these models, or recognizing their suitability for operational purposes, is of paramount importance for providing valid solutions to real problems in our society. These problems may be related, for instance, to ocean transport phenomena, such as oil spills, chemical or plastic transportation. Uncertainty quantification in this context supports taking appropriate decisions about the use, or not, of a particular data source in these applications.

Ocean models are built on partial differential equations, which are only an approximation of reality. Indeed, typically ocean models approach ocean motion by the Reynolds-averaged Navier–Stokes equations using the hydrostatic and Boussinesq assumptions. In this context inaccurate or inadequate models lead to *structural uncertainty*. Even if these equations were perfectly accurate models, they contain parameters, such as viscosity or diffusivity, which are not known precisely and cause *parameter uncertainty*. Boundary conditions on input variables, lead to *parametric variability*. For instance input variables, such as velocities, experience at the surface atmospheric winds, which impose forcings on the velocities, and these atmospheric forcings are not precisely known. Eventually these models are not solved exactly, but numerically through discretization methods and numerical approximations which are subject to numerical errors, and results in *algorithmic uncertainty*. For all these reasons, the predicted ocean currents are also uncertain. Uncertainties in the system outputs determined from the solutions that result from uncertainties in the system inputs are referred to as *forward uncertainty* [2].

In this work, we are interested in evaluating the reliability of the outputs, i.e. the ocean currents, with respect to the transport that they produce. This is a perspective slightly different to the classical one now described in which ocean model adequacy is judged only against the velocity fields. Transport in the ocean surface is produced by fluid parcels that follow trajectories $\mathbf{x}(t)$ that evolve according to the dynamical system:

$$\frac{d\mathbf{x}}{dt} = \mathbf{v}(\mathbf{x}, t), \tag{1}$$

where the position is described in longitude (λ) and latitude (ϕ) coordinates, that is, $\mathbf{x} = (\lambda, \phi)$, and $\mathbf{v}$ represents the velocity field, which has two components determined by the zonal (u) and meridional (v) velocities. In longitude/latitude coordinates, the dynamical system in Eq. (1) can be rewritten as:

$$\begin{cases} \dfrac{d\lambda}{dt} = \dfrac{u(\lambda, \phi, t)}{R\cos\phi} \\ \dfrac{d\phi}{dt} = \dfrac{v(\lambda, \phi, t)}{R} \end{cases} \tag{2}$$

where R is the Earth's radius. The system (1), which is a general expression encompassing the specific problem dealt with in (2), is a nonlinear non-autonomous dynamical system in 2D. Uncertainties in the velocities $\mathbf{v}(\mathbf{x}, t)$, or more generally in the vector field, produce uncertainties in the solutions $\mathbf{x}(t)$. In general, as illustrated in Fig. 1, the exact model connecting two successive observations is not known. Only the initial observation, $\mathbf{x_0}$, and the final state, $\mathbf{x}^*$, are measurable. They are presented in the red colour in the figure. The evolution of initial conditions, $\mathbf{X_0}$, in a neighbourhood close to the initial observation, $\mathbf{x_0}$, towards a final state, $\mathbf{X}^*$, predicted by a model is expressed with the pink colour in the same figure. The uncertainty of the model in representing the observations can be expressed in a number of ways. It may be defined by an absolute error E, which measures distance, in a certain metrics, between the final observation $\mathbf{x}^*$, which is considered a target and the computed prediction $\mathbf{X}^*$. This work proposes measures for this error and links the proposed uncertainty quantifier with dynamical objects present in the model (1). This is done without making any mathematical assumption about the observations.

This paper is structured as follows. In Section 2, we will discuss and develop an approach to uncertainty quantification recently taken for an ocean study case in García-Sánchez et al. [3]. We will show evidence of connections between the introduced definitions and the dynamical objects of system (1). In Section 3, we will provide formal results to show how, for specific simple examples of the system (1), the definition of uncertainty quantification given in Section 2 is able to high-

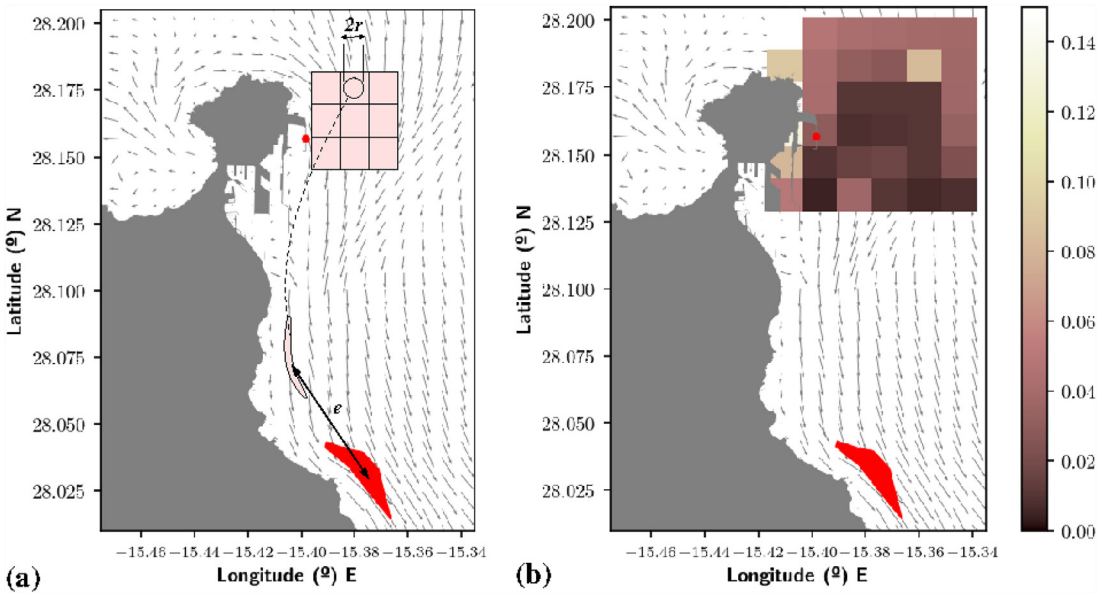

Fig. 2. A graphical representation of the uncertainty quantification in a neighbourhood of the accident location (red dot) with respect to a target (the red blob). a) A schematic representation of Eq. (3) computation for an initial pink blob with radius r and its evolution; b) results of the computation of Eq. (3) for different initial blobs of radius $r = 3.5 \times 10^{-3}(^\circ)$ placed in the center of each cell in the meshgrid. The colourmap is expressed in degree values for the final distances to the target.

light these dynamical objects. These results support one of the main findings of this article, which is that stable invariant manifolds of hyperbolic trajectories provide a *structure* to forward uncertainty quantification. We will see in detail what is meant by this statement. Section 4 presents a discussion with further examples that illustrate the findings of this work and links uncertainty quantification to Lagrangian Descriptors and other Lagrangian indicators found in the literature. Finally, in Section 5, we discuss our conclusions.

2. Transport uncertainty quantification in ocean models

In this section we propose uncertainty quantification metrics. We work in the context of transport in ocean models, beginning the discussion from the results presented in García-Sánchez et al. [3], which considers the performance of very high resolution tools for the monitoring and assessment of environmental hazards in coastal areas. In particular, this work, following the scheme presented in Fig. 1, quantifies uncertainties of several high resolution hydrodynamic models in the area of Gran Canaria by measuring an error between the observations and predictions for the evolution of a diesel fuel spill event, well documented by port authorities and tracked with very high resolution remote sensing products. The pollution event was produced after the collision of the passenger ferry 'Volcán de Tamasite' with the Nelson Mandela dike in La Luz Port on April 2017. After the crash, supply pipes along the dike were broken and diesel fuel poured into the sea. SAR Sentinel 1 images were available in the area approximately one day and a half after the accident from which it was possible to identify the spill. For that period ocean currents in the area were available from two sources. One was the Copernicus Marine Service model for the Iberian–Biscay–Irish region (CMEMS IBI-PHY, IBI hereafter) and other was a very high resolution model of Puerto de la Luz setup by Puertos del Estado currently implemented and running operationally in different Spanish Port Authorities within the SAMOA port forecast system [4]. In [3], for each model, uncertainties were quantified by measuring an error with respect to a target, a 'ground truth', which should be recovered by the model. In particular, following the scheme proposed in Figs. 1 and 2 illustrates how the uncertainty quantifier metrics is proposed. The ferry impact point, the Nelson Mandela dike, which is marked with the red dot, represents an initial observation. The currents represented in the background are the ones obtained from the model set by Puertos del Estado at day t_0. The elongated red blob represents the spill as identified from satellite images one day and a half after the accident. This is the target observation, the 'ground truth'. In panel (a) a set of initial conditions, $\mathbf{X_0}$, is selected in the neighbourhood of the initial observation and marked in a rectangular pink domain. This domain is divided into sub-domains and in each one a small circular blob with radius $r = 3.5 \times 10^{-3}(^\circ)$, is evolved in a time interval from the initial time t_0. This is represented just for one of the sub-domains. The blob distorts while it approaches the target observed spill. A way to measure the 'proximity' between the blob and the target spill at the final time, t^*, is to compute the distance between the centroid of the evolved blob, ($\mathbf{c}_m$), and that of the observed spill, ($\mathbf{c}_g^*$). Mathematically this can be expressed as:

$$e(t^*) = \|\mathbf{c}_m(t^*) - \mathbf{c}_g^*\|. \tag{3}$$

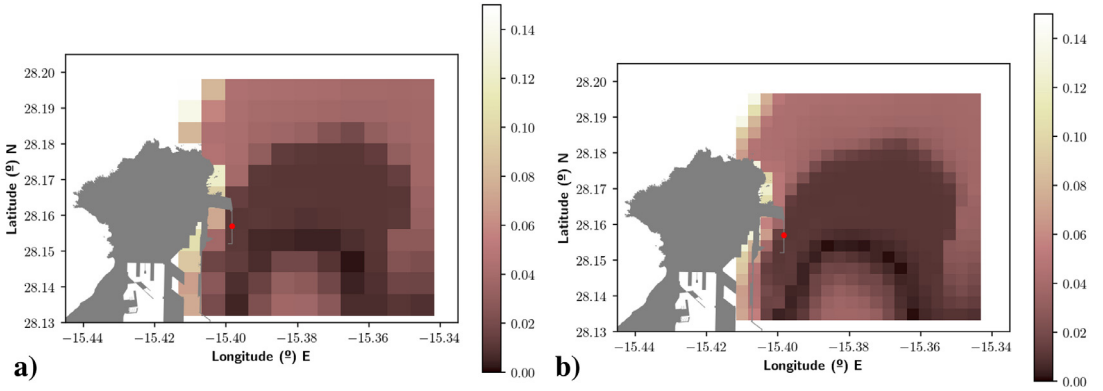

Fig. 3. A quantitative measure of uncertainty for the Puertos del Estado model for la Luz Port, based on errors measured as distances to the target 'ground truth' spill. Higher colour-map values correspond to larger errors or uncertainties. The accident location is marked with a red asterisk. a) Uncertainties computed on a 11×11 mesh considering initial blobs with radius $r = 3.5 \times 10^{-4}(^\circ)$; b) uncertainties associated with a 20×20 mesh considering initial blobs with radius $r = 3.5 \times 10^{-5}(^\circ)$.

Here, $\|\cdot\|$ denotes the modulus of the vector. The position of the centroid of the evolved spill, $\mathbf{c}_m$, depends on time t, while the centroid of the ground value slick $\mathbf{c}_g^*$ does not, since it is an observation at a final time, t^*. The centroid of a finite set of N points $\{\mathbf{x}_k\}_{k\in\mathbb{N}} \in \mathbb{R}^n$ is defined as:

$$\mathbf{c} = \frac{1}{N}\sum_{k=1}^{N}\mathbf{x}_k, \tag{4}$$

where $\mathbf{x}_k$ are the (lon, lat) coordinates that define the contour of the slick in an equirectangular projection. The solid black line e in panel (a) is the distance between centroids of the modelled and observed blobs. This is the value taken by Eq. (3). The procedure is repeated for additional circles centered in different positions of the sub-domains or cells, in the neighbourhood of the accident. The evolution of each of these circular blobs is different due to the chaotic nature of transport in this setting. Panel (b) in Fig. 2 provides a visualization on how this calculation changes in each sub-domain. This panel represents a colourmap which is placed in the port neighbourhood, at the same position than the pink domain in panel (a). It considers a 6×6 mesh-grid, and the colourcode within each cell represents the value of Eq. (3) obtained for blobs with initial positions in the center of each cell and initial radius of $r = 3.5 \times 10^{-3}(^\circ)$. We observe a nonuniform distribution.

Fig. 3 expands results of Fig. 2b) by increasing the number of cells in the neighbourhood domain and decreasing the radius of each initial blob. In particular, Fig. 3a) considers a mesh 11×11 and initial blobs with radius $r = 3.5 \times 10^{-4}(^\circ)$. Fig. 3b) increases the number of cells to a 20×20 mesh-grid and decreases the radius of initial blobs to $3.5 \times 10^{-5}(^\circ)$. Fig. 3b) makes visible an underlying structure which is directly related to the invariant dynamical structures, as we will shown later. In the limit $r \to 0$, expression (3) is rewritten as:

$$L_{UQ}(t^*) = \|\mathbf{x}(t^*) - \mathbf{c}_g^*\|. \tag{5}$$

where $\mathbf{x}(t)$ is a trajectory of a fluid parcel, a solution to the system (1), with initial position $\mathbf{x}_0$ at each cell in the grid. Fig. 4a) illustrates the results of this calculation in a very fine grid. In a perfect model one would have expected that minimum uncertainty values would have been placed close to the point in which the accident occurred, however Figs. 3 and 4 a) do not show that, justifying that L_{UQ} is represented not just at the spill point, but in a domain close to it in order to gain insights into the quality of the model near the initial observation. Next we discuss the distribution of minimum uncertainty values in this neighbourhood and its interpretation.

One of the goals of this paper is to establish connections between invariant dynamical objects that control transport in vector fields obtained from models and the uncertainty quantifier (5). The former are geometrical objects that organize the evolution of modelled particles schematically into regions corresponding to qualitatively distinct dynamical behaviours. In the context of fluid dynamics these objects are referred to as Lagrangian Coherent Structures (LCS). An essential ingredient of the LCS are hyperbolic trajectories characterized by high contraction and expansion rates. Directions of contraction and expansion define, respectively, stable and unstable directions, which are, respectively, related to the stable and unstable manifolds. In the context of the ocean model and the event described above, Garcia-Sánchez et al. have shown in García-Sánchez et al. [3] that there exists a hyperbolic trajectory located on the coastline very close to the accident point, in a detachment configuration, which is related to the phenomena of flow separation. Under this configuration, the stable manifold of the hyperbolic trajectory is aligned with the coast, and the unstable manifold is transversal to it. Fig. 5 illustrates, respectively, in blue and red the stable and unstable manifolds of the separation trajectory for the studied case on the date the accident occurred. In the model any blob placed in the neighbourhood of the separation trajectory, eventually evolves to become aligned with the unstable manifold, which is an attracting material curve. Fig. 6 shows the consistency between the model and observations. Indeed, the observed spill (in red) has evolved to become completely aligned with the unstable

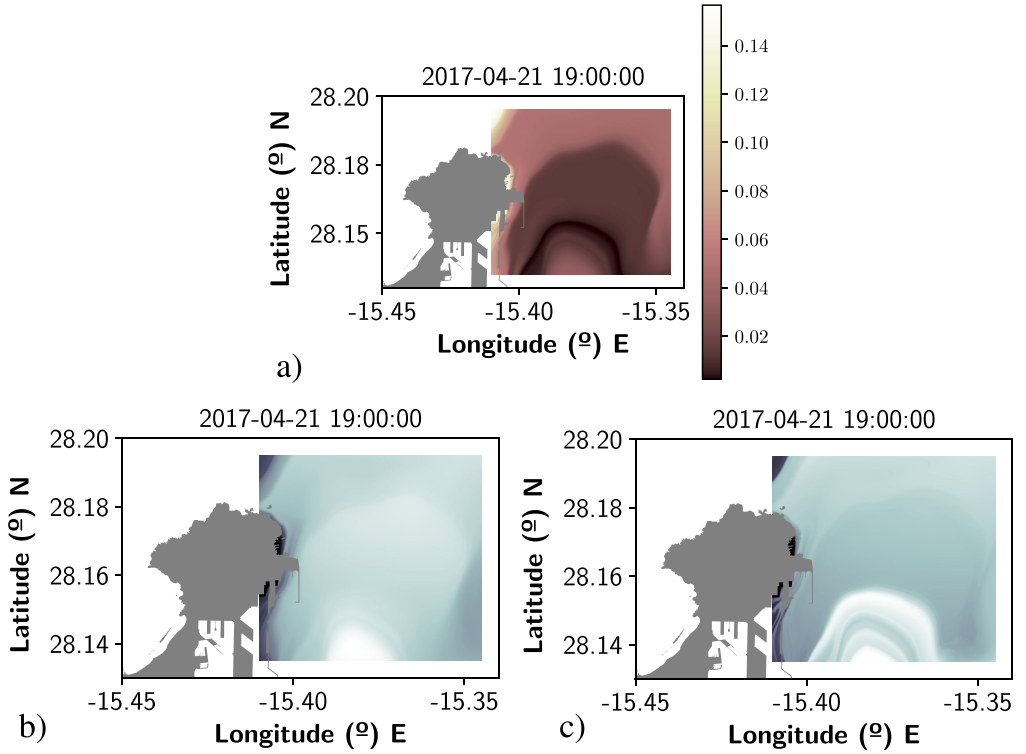

Fig. 4. a) Evaluation of the Lagrangian uncertainty quantifier given in Eq. (5); b) stable manifolds as revealed by the M function (7) using $\tau = 1.5$ days; c) stable manifolds as revealed by the M function using $\tau = 2$ days.

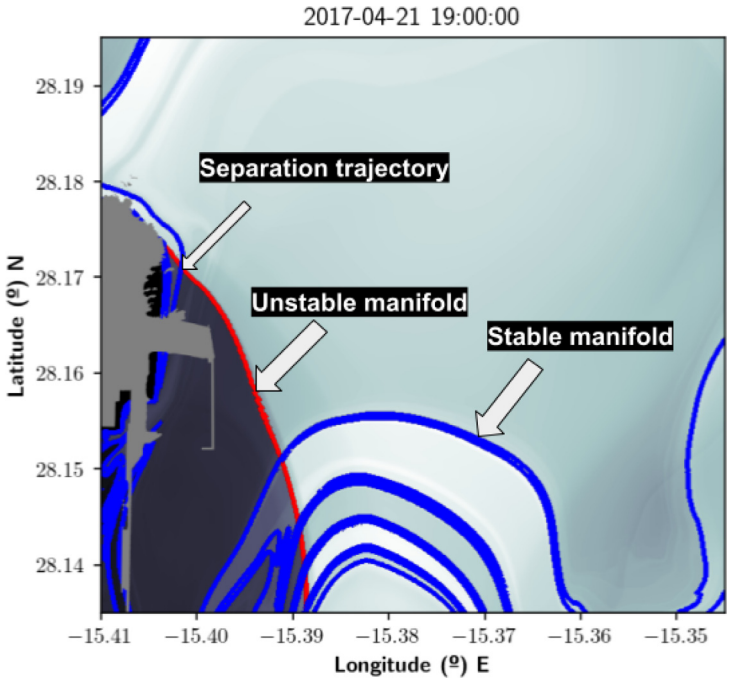

Fig. 5. The Lagrangian skeleton of the ocean model on the accident day, the 21 April 2017 at 19:30h. LCSs are highlighted by the red and blue colours over the gray in the background.

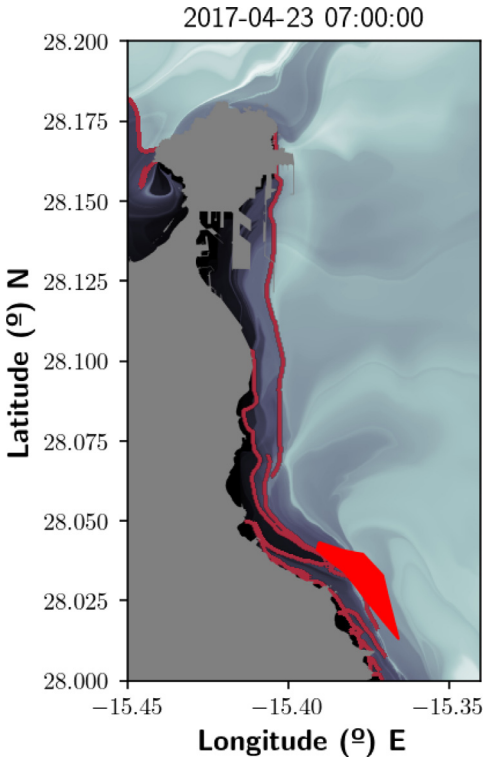

Fig. 6. The Lagrangian skeleton of the ocean model on the 23rd April 2017 at 7:00 a.m, and the observed position of the spill according to satellite images (red blob). Unstable manifolds are highlighted by the red colour over the gray in the background.

manifold. The technical justification underlying this behaviour would be the Inclination Lemma (also called the λ-Lemma) [5,6] that roughly says that successive images of any disc transverse to the stable manifold of a hyperbolic fixed point eventually accumulate on the unstable manifold.

The invariant dynamical structures displayed in Fig. 5 have been obtained by means of the Lagrangian Descriptor [7–9], which measures arc-length of trajectories:

$$M = \int_{t_0-\tau}^{t_0+\tau} \left\| \frac{d\mathbf{x}(t)}{dt} \right\| dt. \tag{6}$$

In [10], for some generalizations of the expression (6), and for some specific vector fields, it is proved that stable and unstable manifolds are aligned with singular features of this function. The forward integration highlights the stable manifold, while the backwards integration highlights the unstable manifold. In that work the notion of singular feature is related to an undefined directional derivative in a direction transverse to the manifold curve. In Fig. 5, red and blue curves are placed on the singular features of M. These curves have been computed by processing the field provided by the Lagrangian Descriptor to extract its singular features. The processing is achieved by using the Canny algorithm implemented in the Python library opencv-python. Canny is an algorithm designed for edge detection. It is a basic algorithm for any line edge or contour detection that is accurate and easy to use. Although for the vector field under consideration there is not a formal proof that these lines correspond to stable and unstable manifolds, we refer to them like that because there exist results in the literature [11–13] in which, for vector fields coming from data sets like this one, it has been verified that stable and unstable manifolds are aligned with singular features of M. In those works this has been done by computing manifolds separately, with a high fidelity estimation method described in Mancho et al. [14], 15], 16], which has as its basis the local stable and unstable manifold theorem [14]. Unstable manifolds displayed in Fig. 6 are obtained similarly to those in Fig. 5.

The metric given in (5) possess similarities with the forward definition of the function M:

$$M = \int_{t_0}^{t^*=t_0+\tau} \left\| \frac{d\mathbf{x}(t)}{dt} \right\| dt. \tag{7}$$

The analogy between structures obtained from expressions (5) and (7), is confirmed from Fig. 4. Panel a) displays expression (5) results, while panels b) and c) display Eq. (7) results for $\tau = 1.5$ and 2 days, respectively. Fig. 4 highlights singularities both for the forward uncertainty quantifier and for the forward M function. From this figure it is clear that uncertainties displayed in panel a) reach minimum values along the stable manifold. In this case, since the observed evolution of the spill is aligned with the unstable manifold (see Fig. 6), it is expected that minimum values of the uncertainty

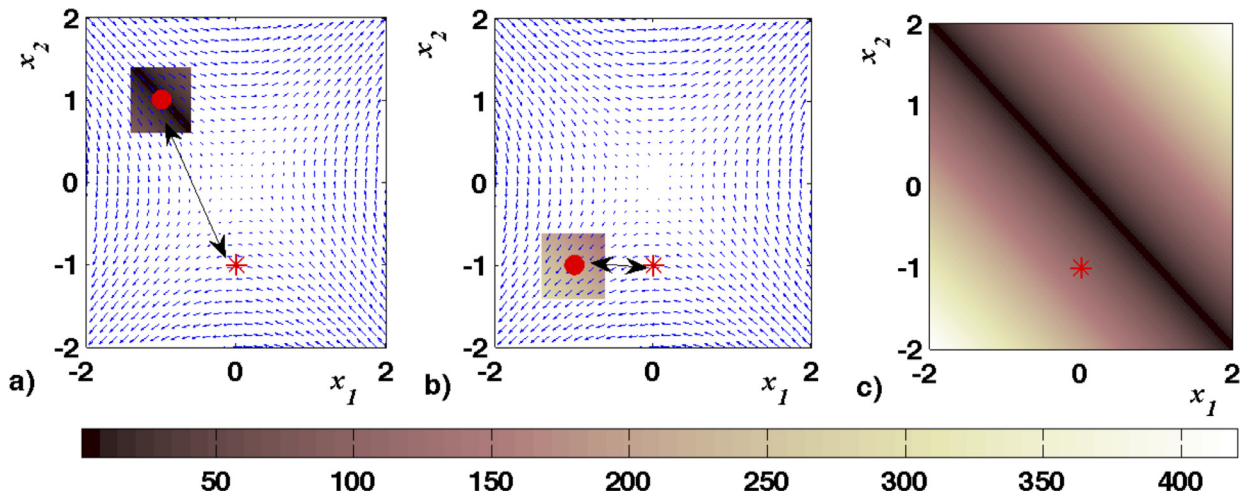

Fig. 7. a) and b) two successive observations at time t_0 (red circle) and time t^* (red asterisk). The transition between them is modelled by the vector field at the background and L_{UQ} is represented in the neighbourhood of the initial observation. Uncertainties are lower for the case a) as confirmed by the colourbar; c) L_{UQ} evaluated in the whole domain. This expresses the uncertainty associated to the planar flow, assuming observations that start in different points of the representation domain and that evolve towards the red asterisk (target position).

quantifier correspond to the stable manifold. Indeed, the stable manifold is an optimal pathway towards the unstable manifold (see the Inclination Lemma quoted above), which in turn is an attracting material curve towards which all modelled fluid parcels evolve after a transition time, and if the model is adequate also will behave this way for observed spills. On the other hand, indicators of *structural uncertainty* that show inadequacy of the model would correspond to situations in which these minimum values are not reached along the stable manifolds. For instance, this would have been the case if the observed spill in Fig. 6 would have been found far from the unstable manifold.

3. Formal results

This section is focused on illustrating the analogies found in Fig. 4 between the pattern in panel a), which is related to uncertainty quantification, and those in panels b) and c), which are related to stable invariant manifolds. For the event described in the previous section computations in panel a) are performed with the measure proposed in Eq. (5) to quantify uncertainty in a neighbourhood of the accident location. When the calculation is performed on a very fine grid it is found that the uncertainty L_{UQ} has a *structure* that is related to that of invariant stable manifolds. In order to find answers to the question of why there are singular structures obtained from the expression (5) that are aligned with invariant stable manifolds of hyperbolic trajectories, we need to assume an explicit expression for the vector field in Eq. (1). Indeed in the example discussed in the previous section, velocities are given as data-sets and this makes difficult to proceed with exact calculations. In this way, in this section we perform an analysis in simplified planar vector fields with exact explicit expressions. Fig. 7 displays such example. In panel a) an initial observation at time t_0 is marked with a red circle. At a later time, t^*, this observation is at the target position marked with a red asterisk. We model this evolution with the vector field at the background, which is represented at time t_0. In order to quantify the uncertainty in the neighbourhood of the initial observation, we display the evaluation of L_{UQ} around it. The colourbar placed at the bottom of the figure, measures the uncertainty in the domain units. This colourbar indicates that uncertainties in this neighbourhood are low. At least lower than those displayed for the experiment in panel b). In this case the initial observation is at a different position, although the target is kept at the same position than in a). In this case uncertainties are larger, indicating that the vector field in the background is not a good model to express the transition between these two observations. Finally panel c) displays L_{UQ} evaluated in the whole domain. This expresses the uncertainty associated to the planar flow, assuming that observations start in different points of the representation domain and that they evolve towards the assumed observed target position at the red asterisk. The panel confirms that model has a better performance for those initial observations placed at the diagonal. Results presented next in this section are displayed following this type of representation.

Our analysis in this section follows the spirit of the work by Mancho et al. [9], Lopesino et al. [10,17], García-Garrido et al. [18]. We assume the definition of singular features given there, by considering that these are features of L_{UQ} on which the transversal derivative is not defined. We will prove, for simple selected examples, that stable manifolds are aligned with those singular features of L_{UQ}.

Finally, before beginning our discussion the definition (5) is generalized as follows:

$$L_{UQ}(\mathbf{x}_0, t, p) = \left[\sum_{i=1}^{n} |x_i(t) - x_i^*|^p\right]^{\frac{1}{p}}, \quad p > 1, \ \mathbf{x}_0 \in \mathbb{R}^n. \tag{8}$$

Here, $\mathbf{x}_0$ is the initial condition of the trajectory $(x_1(t), x_2(t), \ldots, x_n(t))$. In the particular case described in the previous section $n = 2$, which corresponds to the ocean surface, and $p = 2$. The coordinates of the target $\mathbf{c}_g^*$ are (x_1^*, x_2^*) An alternative for this expression that we will use is the following:

$$L_{UQ}(\mathbf{x}_0, t, p) = \sum_{i=1}^{n} |x_i(t) - x_i^*|^p, \ \ p \leq 1, \ \ \mathbf{x}_0 \in \mathbb{R}^n. \tag{9}$$

3.1. The autonomous saddle point

The first example that we analyze is the vector field that corresponds to the Hamiltonian linear saddle case for which $\mathbf{x} \in \mathbb{R}^2$, satisfying $\mathbf{x} = (x, y)$ and the equations of motions are:

$$\begin{aligned} \frac{dx}{dt} &= \lambda x, \\ \frac{dy}{dt} &= -\lambda y, \end{aligned} \tag{10}$$

where $\lambda > 0$. For any initial observation (x_0, y_0), we consider the unique solution of this system passing through the condition (x_0, y_0), which is:

$$\begin{cases} x(t) = x_0 e^{\lambda t} \\ y(t) = y_0 e^{-\lambda t}, \end{cases} \qquad \lambda > 0 \tag{11}$$

For this example, the origin (0,0) is a hyperbolic fixed point with stable and unstable manifolds:

$$W^s(0,0) = \{(x, y) \in \mathbb{R}^2 : x = 0, y \neq 0\}, \tag{12}$$

$$W^u(0,0) = \{(x, y) \in \mathbb{R}^2 : x \neq 0, y = 0\}, \tag{13}$$

For simplicity we assume, without loss of generality, that $t_0 = 0$ (this is possible for autonomous systems). We consider the target in the position (x^*, y^*) and apply (11) to (9) to obtain:

$$L_{UQ}(\mathbf{x}_0, t, p) = |x_0 e^{\lambda t} - x^*|^p + |y_0 e^{-\lambda t} - y^*|^p.$$

Regrouping terms, we get

$$L_{UQ}(\mathbf{x}_0, t, p) = |x_0|^p \omega^{-p} |1 - a\omega|^p + |y_0|^p |\omega - b|^p, \ \text{where } a = \frac{x^*}{x_0}, b = \frac{y^*}{y_0}. \tag{14}$$

In this expression, $\omega = e^{-\lambda t}$, which always satisfies $\omega > 0$. We explore separately the first and second terms. For the factor $|1 - a\omega|^p$ there exists a t_L such that if $t > t_L$, then $a\omega << 1$ and $(1 - a\omega) > 0$. This is always the case for $a < 0$ and is a plausible assumption for $a > 0$, if $a << \omega^{-1}$. We recall that $a = x^*/x_0$ and that therefore such t_L exists if $x_0 \neq 0$. In this case positiveness is guaranteed for sufficiently large t, i.e, a Taylor series around $\omega = 0$, attained if $t \gg 1$ and $t > t_L$, is performed for the binomial:

$$(1 - a\omega)^p = 1 - ap\omega + \frac{1}{2}a^2(p-1)p\omega^2 - \frac{1}{6}\omega^3\left(a^3(p-2)(p-1)p\right) + O\left(\omega^4\right).$$

Therefore,

$$\frac{1}{\omega^p}(1 - a\omega)^p = \omega^{-p} + ap\omega^{(1-p)} + \frac{1}{2}a^2(p-1)p\omega^{(2-p)} + O\left(\omega^{(3-p)}\right).$$

We recall that $p \leq 1$ and $\omega = e^{-\lambda t}$. This yields,

$$|x_0|^p |e^{\lambda t} - a|^p = |x_0|^p e^{\lambda t p} + O\left(|x_0|^p a e^{-\lambda t(1-p)}\right).$$

We analyse next the second term in Eq. (14). The sign of $(\omega - b)$ depends crucially on the sign of b given that for $t \gg 1$ the term ω can be as small as we like. Let us consider t_L such that if $t > t_L$ and $b < 0$, then $(e^{-\lambda t} - b) > 0$. The following is valid for t above this lower value:

$$|\omega - b|^p = (\omega - b)^p = (-b)^p + p\omega(-b)^{p-1} + \frac{1}{2}(p-1)p\omega^2(-b)^{p-2}$$

$$+\frac{1}{6}(p-2)(p-1)p\omega^3(-b)^{p-3} + O\left(\omega^4\right)$$

Therefore, when $t \gg 1, b < 0$ and $e^{-\lambda t} \ll 1$,

$$(\omega - b)^p = (-b)^p + O\left(e^{-\lambda t}\right),\ e^{-\lambda t} \ll 1 \tag{15}$$

Now, we consider $b > 0$ and $t > t_L$ satisfying $(\omega - b) < 0$. Therefore:

$$|\omega - b|^p = (-\omega + b)^p = b^p + p\omega b^{p-1} + \frac{1}{2}(p-1)p\omega^2 b^{p-2}$$

$$+\frac{1}{6}(p-2)(p-1)p\omega^3 b^{p-3} + O\left(\omega^4\right).$$

Therefore, when $t \gg 1, b > 0$ and $e^{-\lambda t} \ll 1$,

$$(-\omega + b)^p = b^p + O(\omega). \tag{16}$$

Finally, we conclude that

$$|\omega - b|^p = |b|^p + O\left(e^{-\lambda t}\right),\ \omega \ll 1. \tag{17}$$

Therefore, since $b = y^*/y_0$

$$|y_0|^p |e^{-\lambda t} - b|^p = |y^*|^p + O\left(|y_0|^p e^{-\lambda t}\right),\ e^{-\lambda t} \ll 1.$$

Thus, we can approximate L_{UQ} as

$$L_{UQ}(\mathbf{x}_0, t, p) \approx |x_0 e^{\lambda t}|^p + |y^*|^p = |x_0|e^{\lambda t p} + |y^*|^p \tag{18}$$

where the dominant term is $|x_0|^p e^{\lambda t p}$. Hence, to leading order, the stable manifold at $x = 0$ is aligned with a singular feature of L_{UQ} for 'sufficiently large' t. This statement however must be considered in the sense that expression (18) expresses a good approximation for L_{UQ} as far as $x_0 \neq 0$, and that for any $|x_0| > 0$ is valid for a sufficient large t satisfying, $t > t_L$.

We have shown that Eq. (9) is able to highlight the stable manifolds for the autonomous saddle point. Next, we analyse what happens when we consider Eq. (8), and in which cases it provides information about the stable manifold of the autonomous saddle point. When we apply (11) to (8), it yields

$$L_{UQ}(\mathbf{x}_0, t, p) = \left[|x_0 e^{\lambda t} - x^*|^p + |y_0 e^{-\lambda t} - y^*|^p\right]^{1/p}.$$

We remark that our following calculations will be restricted to $p > 1$ and integer. Rewriting the expression for $\omega = e^{-\lambda t}$

$$L_{UQ}(\mathbf{x}_0, t, p) = \left[\left|\frac{x_0}{\omega}\right|^p |1 - a\omega|^p + |y_0|^p |\omega - b|^p\right]^{1/p} = \left|\frac{x_0}{\omega}\right|\left[|1 - a\omega|^p + \left|\frac{y_0}{x_0}\right|^p \omega^p |\omega - b|^p\right]^{1/p} \tag{19}$$

Recalling that $p > 1, \omega > 0$ and that $(1 - a\omega) > 0$ for sufficiently small ω, i.e. sufficiently large t, and the case $b < 0$ and $(\omega - b) > 0$, a Taylor series around $\omega = 0$, for p integer number, for the second factor:

$$L_{UQ}(\mathbf{x}_0, t, p) = \left|\frac{x_0}{\omega}\right|\left[1 - a\omega + \left|\frac{y_0}{x_0}\right|^p (-b)^p \frac{\omega^p}{p} + O(\omega)^{p+1}\right] \tag{20}$$

Alternatively, considering the case $b > 0$ and $(\omega - b) < 0$, a Taylor series around $\omega = 0$ for the second factor is as follows:

$$L_{UQ}(\mathbf{x}_0, t, p) = \left|\frac{x_0}{\omega}\right|\left[1 - a\omega + \left|\frac{y_0}{x_0}\right|^p (b)^p \frac{\omega^p}{p} + O(\omega)^{p+1}\right] \tag{21}$$

Therefore in general:

$$L_{UQ}(\mathbf{x}_0, t, p) = \left|\frac{x_0}{\omega}\right|\left[1 - a\omega + \left|\frac{y_0}{x_0}\right|^p |b|^p \frac{\omega^p}{p} + O(\omega)^{p+1}\right]$$

$$= \left|\frac{x_0}{\omega}\right| - a|x_0| + |y_0|^p |x_0|^{1-p} \frac{|b|^p}{p}\omega^{p-1} + O(\omega)^p \tag{22}$$

We notice that since $p > 1$, the terms ω^{p-1}, ω^p have positive exponents and if $\omega \ll 1$ in principle are much smaller than the first term ω^{-1} and therefore:

$$L_{UQ}(\mathbf{x}_0, t, p) \sim \frac{1}{p}\left|\frac{x_0}{\omega}\right|,\ \omega \ll 1 \tag{23}$$

Hence, the stable manifold at $x = 0$ is aligned with a singular feature of this approximation to L_{UQ} for 'sufficiently large' t. This statement though, must be considered with care, because in Eq. (22) the terms in ω^{p-1}, ω^p, are multiplied by $|x_0|^{1-p}$ which has a negative exponent, and therefore have a singularity at $x_0 = 0$. For this reason neglecting these terms versus the first one if we are very close to $x_0 = 0$ would require checking that the products, such as, $|x_0|^{1-p}\omega^{p-1}$ are really small. This implies that Eq. (23) is correctly approximating L_{UQ} for $\omega \ll 1$ as far as we are sufficiently away from 0 in x_0, i.e. $|x_0|^{1-p}\omega^{p-1} \ll 1 \Rightarrow \omega^{p-1} \ll |x_0|^{p-1}$. In practice this condition is satisfied for any grid (x_0, y_0) used in later figures that exclude $x_0 = 0$. Also we can state that for sufficiently large t, L_{UQ} is very close in almost all the domain to the function given in Eq. (23), which possess a "singular feature" aligned with the stable manifold. Fig. 8a) and b), illustrates how the stable manifold is aligned with singular features of the Lagrangian uncertainty quantifier defined either by Eq. (8) or (9).

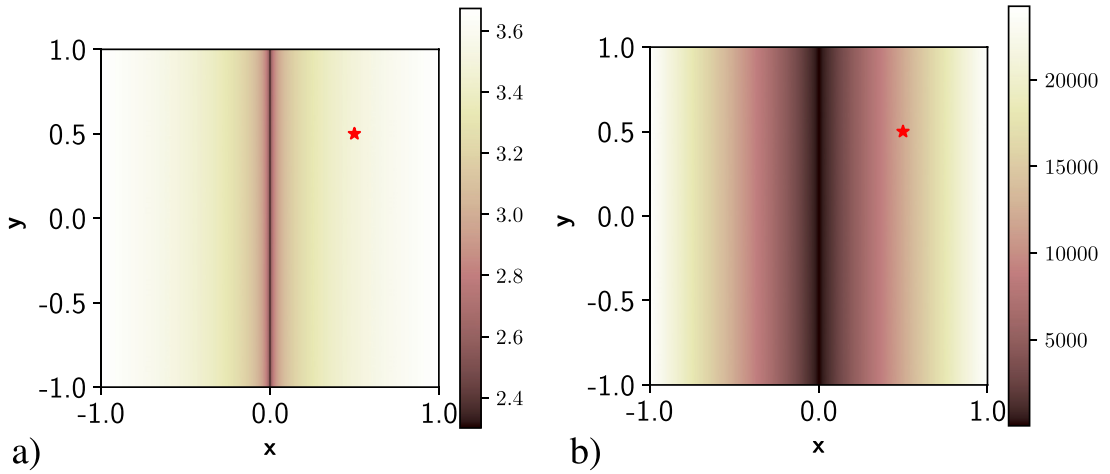

Fig. 8. A representation of Eqs. (8) and (9) for $t^* = 10$ and target $(x^*, y^*) = (0.5, 0.5)$ (red asterisk) for the Hamiltonian linear saddle vector field. a) $p = 2$; b) $p = 0.1$. It can be appreciated how the stable manifold is aligned with a singular feature.

3.2. The autonomous rotated saddle point

This second case that we explore is the vector field of the rotated linear saddle for which the equations of motion are:

$$\begin{cases} \dot{x} = \lambda y \\ \dot{y} = \lambda x, \end{cases} \qquad \lambda > 0 \tag{24}$$

The general solution to this system is:

$$\begin{cases} x(t) = ae^{\lambda t} + be^{-\lambda t} \\ y(t) = ae^{\lambda t} - be^{-\lambda t}, \end{cases} \qquad \lambda > 0 \tag{25}$$

where a and b depend on the initial conditions x_0 and y_0 as follows:

$$a = \frac{x_0 + y_0}{2}, \quad b = \frac{x_0 - y_0}{2}.$$

Here, $a = 0$ corresponds to the stable manifold of the hyperbolic fixed point placed at the origin and $b = 0$ corresponds to its unstable manifold.

For any initial observation (x_0, y_0) and final target observation (x^*, y^*), we introduce the solution (25) into Eq. (9) obtaining:

$$L_{UQ}(\mathbf{x}, t, p) = |ae^{\lambda t} + be^{-\lambda t} - x^*|^p + |ae^{\lambda t} - be^{-\lambda t} - y^*|^p \tag{26}$$

We expand next the first term in Eq. (26). In particular, we consider the case in which $a > 0$ for which it is always possible to find a $t > t_L$ in which $(ae^{\lambda t} + be^{-\lambda t} - x^*) > 0$:

$$|ae^{\lambda t} + be^{-\lambda t} - x^*|^p = (ae^{\lambda t} + be^{-\lambda t} - x^*)^p = \left(\frac{a}{\omega} + b\omega - x^*\right)^p$$

$$= \omega^{-p}\left(a + b\omega^2 - x^*\omega\right)^p,$$

Here we have used $\omega = e^{-\lambda t}$. The Taylor expansion of the binomial when $\omega \ll 1$, i.e., when $t \gg 1$, is

$$\omega^{-p}\left(a + b\omega^2 - x^*\omega\right)^p = \omega^{-p}\Big[a^p - p\omega x^* a^{p-1} + \omega^2\left(bpa^{p-1} + \frac{1}{2}(p-1)p(x^*)^2 a^{p-2}\right)$$

$$-\frac{1}{6}\omega^3\left((p-1)px^* a^{p-3}\left(6ab + p(x^*)^2 - 2(x^*)^2\right)\right) + O\left(\omega^4\right)\Big].$$

Therefore,

$$\omega^{-p}\left(a + b\omega^2 - x^*\omega\right)^p = a\omega^{-p} - p\omega x^* a^{p-1} + \omega^{(2-p)}\left(bpa^{p-1} + \frac{1}{2}(p-1)p(x^*)^2 a^{p-2}\right)$$

$$-\frac{1}{6}\omega^{(3-p)}\left((p-1)px^* a^{p-3}\left(6ab + p(x^*)^2 - 2(x^*)^2\right)\right) + O\left(\omega^{(4-p)}\right)$$

Since $p<1, \omega^{(n-p)} \ll 1$ for $n>1$ when $t \gg 1$. Hence,

$$\omega^{-pt}\left(a+b\omega^{2t}-x^*\omega^t\right)^p = a^p\omega^{-pt}+O\left(\omega^{(1-p)t}\right).$$

By removing the change of variable, we obtain

$$\left(ae^{\lambda t}+be^{-\lambda t}-x^*\right)^p = a^pe^{\lambda pt}+O\left(e^{-(1-p)\lambda t}\right) \approx a^pe^{\lambda pt}, \text{ when, } t \gg 1. \tag{27}$$

We consider now the case $a<0$ that implies $\left(ae^{\lambda t}+be^{-\lambda t}-x^*\right)<0$ for some sufficiently large t. The Taylor series is the same, except for a minus sign. It yields,

$$\left(ae^{\lambda t}+be^{-\lambda t}-x^*\right)^p = -a^pe^{\lambda pt}-O\left(e^{-(1-p)\lambda t}\right) \approx -a^pe^{\lambda pt}, \text{ when, } t \gg 1. \tag{28}$$

Finally,

$$|ae^{\lambda t}+be^{-\lambda t}-x^*|^p = |a|^pe^{\lambda pt}+O\left(e^{-(1-p)\lambda t}\right) \approx |a|^pe^{\lambda pt}, \text{ when, } t \gg 1. \tag{29}$$

We analyse next the second term in Eq. (26). As before, we start considering the case $a>0$ and $(ae^{\lambda t}-be^{-\lambda t}+y^*)>0$. After making the change of variable $\omega = e^{-\lambda t}$ we obtain:

$$\omega^{-p}\left(a-b\omega^2-y^*\omega^t\right)^p = \omega^{-p}\Big[a^p-p\omega^ty^*a^{p-1}-\frac{1}{2}\omega^2\left(pa^{p-2}\left(2ab-p(y^*)^2+(y^*)^2\right)\right) + \frac{1}{6}(p-1)p\omega^3y^*a^{p-3}\left(6ab-p(y^*)^2+2(y^*)^2\right)+O\left(\omega^4\right)\Big].$$

Since $p<1, \omega^{(n-p)} \ll 1$ for $n>1$ when $t \gg 1$. Hence,

$$\omega^{-p}\left(a-b\omega^2+y^*\omega\right)^p = a^p\omega^{-p}+O\left(\omega^{(1-p)}\right).$$

By removing the change of variable, we obtain:

$$\left(ae^{\lambda t}-be^{-\lambda t}-y^*\right)^p = a^pe^{\lambda pt}+O\left(e^{-(1-p)\lambda t}\right) \approx a^pe^{\lambda pt}, \text{ when, } t \gg 1. \tag{30}$$

We compute the same term but in the case $a<0\left(ae^{\lambda t}-be^{-\lambda t}-y^*\right)<0$. The Taylor series is the same, except for a minus sign. It yields,

$$\left(ae^{\lambda t}-be^{-\lambda t}-y^*\right)^p = -a^pe^{\lambda pt}-O\left(e^{-(1-p)\lambda t}\right) \approx -a^pe^{\lambda pt}, \text{ when, } t \gg 1. \tag{31}$$

Finally,

$$|ae^{\lambda t}-be^{-\lambda t}-y^*|^p = |a|^pe^{\lambda pt}+O\left(e^{-(1-p)\lambda t}\right) \approx |a|^pe^{\lambda pt}, \text{ when, } t \gg 1. \tag{32}$$

Thus,

$$L_{UQ} = |ae^{\lambda t}+be^{-\lambda t}-x^*|^p+|ae^{\lambda t}-be^{-\lambda t}+y^*|^p \approx |a|^pe^{\lambda pt}, \text{ when, } t \gg 1. \tag{33}$$

The stable manifold at $a=0$ is aligned with a singular feature also at $a=0$.

As for Eq. (8) considering $p>1$ and $\omega = e^{-\lambda t}$ leads:

$$\begin{aligned} L_{UQ} &= \left[|ae^{\lambda t}+be^{-\lambda t}-x^*|^p+|ae^{\lambda t}-be^{-\lambda t}+y^*|^p\right]^{1/p} \\ &= \omega^{-1}\left[|a+b\omega^2-x^*\omega|^p+|a-b\omega^2+y^*\omega|^p\right]^{1/p} \\ &= 2^{\frac{1}{p}}|a|\omega^{-1}-2^{-1+\frac{1}{p}}(2b+x^*-y^*)+2^{-3+\frac{1}{p}}|a|^{-1}\cdot \\ &\quad (4ab+(-1+p)(-2b+x^*+y^*)^2)\omega+O(\omega)^2 \end{aligned} \tag{34}$$

As before the leading term in ω leads to:

$$L_{UQ} \sim 2^{\frac{1}{p}}|a|\omega^{-1} \tag{35}$$

and similar considerations apply in neglected terms to the ones made for Eq. (22), but now regarding to singularities at $a=0$. Fig. 9a) and b), illustrate how the stable manifold is aligned with singular features of the Lagrangian uncertainty quantifier defined either by Eq. (8) or (9).

3.3. Discrete maps

These findings in the previous two subsections can be easily extended to discrete time dynamical systems, which are also useful in applications. Discrete time dynamical systems are defined as maps.

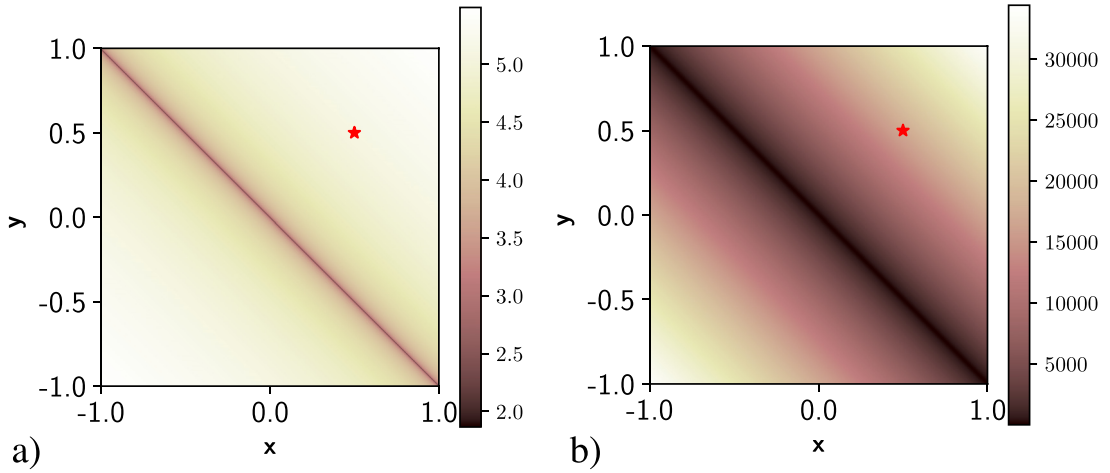

Fig. 9. A representation of Eqs. (8) and (9) for $t^* = 10$ and target $(x^*, y^*) = (0.5, 0.5)$ (red asterisk) for the rotated linear saddle vector field for a) $p = 2$; b) $p = 0.1$. It can be appreciated how the stable manifold is aligned with a singular feature.

The autonomous saddle point

Consider the following linear, area-preserving autonomous map:

$$\begin{cases} x_{n+1} = \lambda x_n \\ y_{n+1} = \frac{1}{\lambda} y_n, \end{cases} \qquad \lambda > 1. \tag{36}$$

For an initial condition (x_0, y_0), the unique solution of this system is:

$$\begin{cases} x_n = x_0 \lambda^n \\ y_n = y_0 \lambda^{-n}, \end{cases} \qquad \lambda > 1. \tag{37}$$

As for the continuous time case, the origin (0,0) is a hyperbolic fixed point with stable and unstable manifolds:

$$W^s(0,0) = \{(x,y) \in \mathbb{R}^2 : x = 0, y \neq 0\}, \tag{38}$$

$$W^u(0,0) = \{(x,y) \in \mathbb{R}^2 : x \neq 0, y = 0\}, \tag{39}$$

We apply (37) to (9) to obtain:

$$L_{UQ}(\mathbf{x}, n, p) = |x_0 \lambda^n - x^*|^p + |y_0 \lambda^{-n} - y^*|^p. \tag{40}$$

Regrouping terms, we get

$$L_{UQ}(\mathbf{x}, n, p) = |x_0|^p |\lambda^n - a|^p + |y_0|^p |\lambda^{-n} - b|^p, \text{ where } a = \frac{x^*}{x_0}, b = \frac{y^*}{y_0}. \tag{41}$$

Considering that the transformation $e^{\lambda t} \to \lambda^n$ can be directly applied to all the calculations performed in the continuous time case, we recover from Eq. (14):

$$L_{UQ} \approx |x_0|^p |\lambda^{np}| + O\left(|\lambda|^{-n(1-p)}\right), \text{ when, } n \gg 1. \tag{42}$$

When $p < 1$, the dominant term is $|x_0|^p \lambda^{np}$. Hence, the stable manifold at $x = 0$ is aligned with singular features of L_{UQ} for 'sufficiently large' iteration n.

The same is applicable to L_{UQ} (8). It yields,

$$L_{UQ} \approx |x_0 \| \lambda^n| + O(1), \text{ when, } n \gg 1 \text{ and } p < 1. \tag{43}$$

We note that the stable manifold at $x = 0$ is aligned with singular features of L_{UQ} for a 'sufficiently large' iteration n. The same issues as before regarding singularities on the manifold position apply.

Fig. 10 a) and b), illustrate how the stable manifold is aligned with singular features of the Lagrangian uncertainty quantifier defined either by Eq. (8) or (9).

The autonomous rotated saddle point

We consider the following discrete dynamical system:

$$F(x,y) = A\begin{pmatrix} x \\ y \end{pmatrix}, \text{ where } A = \frac{1}{2\lambda}\begin{pmatrix} \lambda^2 + 1 & \lambda^2 - 1 \\ \lambda^2 - 1 & \lambda^2 + 1 \end{pmatrix}, \ \lambda > 1. \tag{44}$$

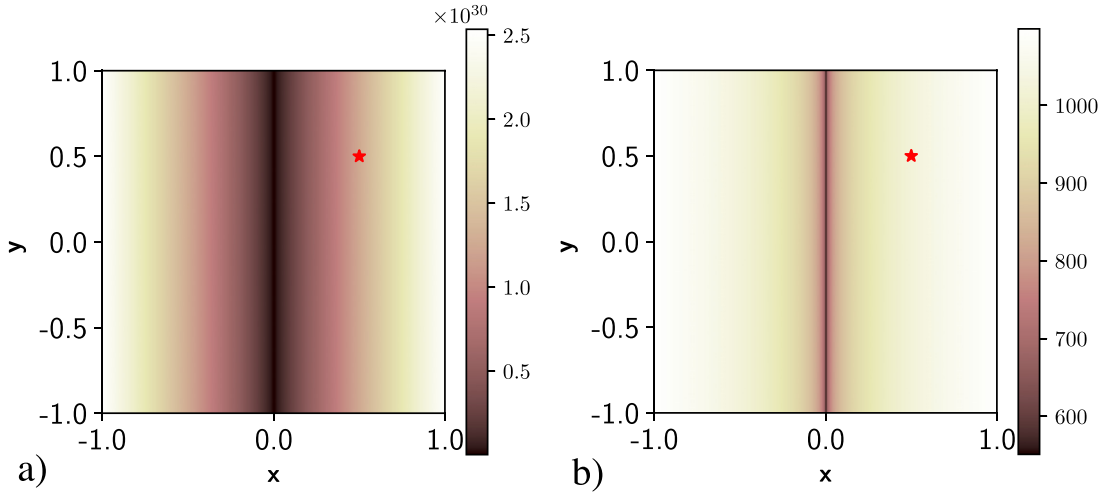

Fig. 10. In Figure a) there is a representation for the autonomous saddle when we apply Eq. (8) for $p = 2$. In b), we illustrate the same representation but for Eq. (9) when $p = 0.1$. It can be appreciated how the stable manifold is aligned with the singular feature.

It is easy to see that the stable and the unstable manifolds are given by the vectors $(1, -1)$ and (1,1) respectively. The solution of this system yields to,

$$\begin{cases} x_n = a\lambda^n + b\lambda^{-n} \\ y_n = a\lambda^n - b\lambda^{-n}, \end{cases} \qquad \lambda > 1 \tag{45}$$

where

$$a = \frac{x_0 + y_0}{2}, \quad b = \frac{x_0 - y_0}{2}.$$

Again considering the transformation $e^{\lambda t} \to \lambda^n$ and the use of previous results for the continuous time case, we recover from Eq. (33):

$$L_{UQ}(\mathbf{x}, n, p) = |a\lambda^n + b\lambda^{-n} - x^*|^p + |a\lambda^n - b\lambda^{-n} - y^*|^p.$$

Therefore, the dominant term is

$$L_{UQ}(\mathbf{x}, n, p) \sim |a|^p |\lambda|^{np}.$$

Since $a = \frac{x_0+y_0}{2}$, there is a singular feature at $x = -y$, i.e., in the subspace generated by $(1, -1)$. Hence, the stable manifold is aligned with a singular feature of L_{UQ}.

The same is applicable to L_{UQ} (8). It yields,

$$L_{UQ}(\mathbf{x}, n, p) \sim |a||\lambda|^n,$$

Hence, the stable manifold is aligned with a singular feature of L_{UQ}. Fig. 11a) and b), illustrates how the stable manifold is aligned with singular features of the Lagrangian uncertainty quantifier defined either by Eqs. (8) or (9).

4. The Duffing equation

Results in the previous sections are generalized to the autonomous nonlinear case by means of the Moser's theorem [19]. This theorem applies to analytic two-dimensional symplectic maps having a hyperbolic fixed point or, similarly, to two-dimensional time-periodic Hamiltonian vector fields having a hyperbolic periodic orbit (which can be reduced to the former case considering a Poincaré map). The case of a Hamiltonian nonlinear autonomous system is a one-parameter family of symplectic maps, and therefore Moser's theorem applies. Following proofs sketched by Lopesino et al. [10,17] results may be extended to the case of non-autonomous nonlinear dynamical systems by utilizing results like the Hartman–Groβman theorem.

This section discusses further results on the Lagrangian Uncertainty Quantifier by considering the evaluation of (8) over a vector field obtained from the nonlinear periodically forced Duffing equation:

$$\begin{aligned} \dot{x} &= y \\ \dot{y} &= x - x^3 + \epsilon \sin t \end{aligned} \tag{46}$$

Prior to discuss outputs of (8) into Eq. (46), we discuss the structure of invariant manifolds of hyperbolic trajectories in Eq. (46) for the case $\epsilon = 0.1$ and the persistence versus this time dependent perturbation of tori present in the unforced

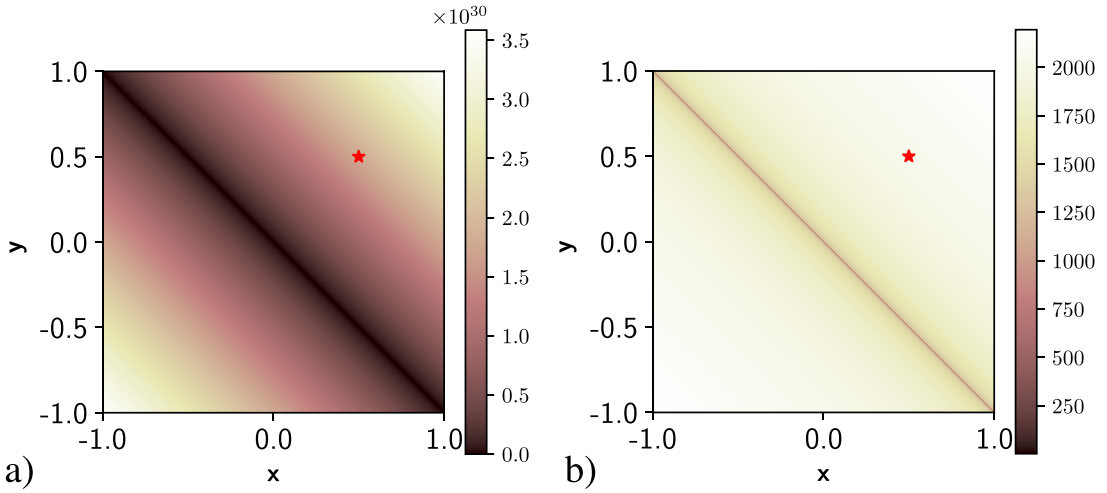

Fig. 11. In Figure a) there is a representation for the rotated saddle when we apply Eq. (8) for $p = 2$. In b), we illustrate the same representation but for Eq. (8) when $p = 0.1$. It can be appreciate how the singular feature is aligned with stable manifold.

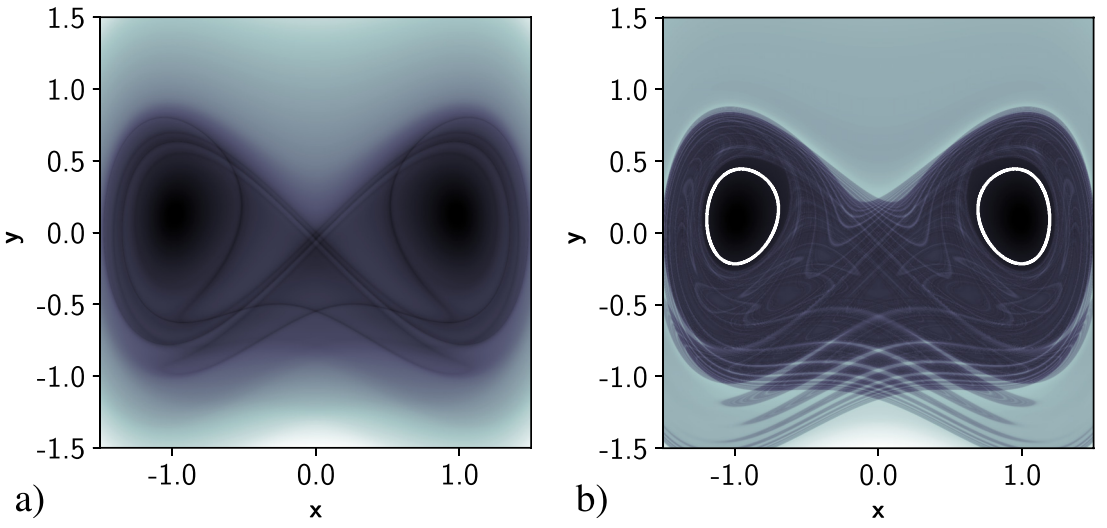

Fig. 12. Evaluation of (6) for the Duffing Eq. (46) at $t_0 = 0$. a) $\tau = 10$; b) $\tau = 50$. At this τ the average of M in the smooth regions has converged and the level curve represent and invariant tori.

version of Eq. (46), i. e, $\epsilon = 0$. In the perturbed case, the hyperbolic fixed point placed at the origin, becomes a hyperbolic periodic trajectory [7], and their stable and unstable manifold can be highlighted by the Eq. (6) appeared in Section 2 [9]. Additionally, as discussed in Lopesino et al. [10] a scale factor $1/(2\tau)$ applied to (6) converts the expression to an average, which in compact Hamiltonian systems like (46) converges for $\tau \to \infty$ and when this convergence is observed, level curves correspond to invariant structures of the dynamical system. Convergence of means are computationally verifiable on tori, however on hyperbolic sets as discussed in García-Garrido et al. [18], rounding computational errors practically prevent convergence.

Fig. 12 illustrates these points. Panel a) shows invariant manifolds related to the hyperbolic trajectory that are obtained from (6) for $\tau = 10$. These structures become much more rich for larger τ as panel b) confirms. In this panel since the average of M has converged in the smooth region, level curves in the area highlight tori. The outputs of Fig. 12a) may be split into two figures, by separating the backwards and forwards integration of Eq. (6), which displays, respectively, the unstable and stable manifolds. These outputs are depicted, respectively, in Fig. 13a) and b).

Fig. 14 shows the evaluation of L_{UQ} as in Eq. (8) with $p = 2$ for $t_0 = 0, t = t_0 + \tau = 10$ and different targets. In panel a) the chosen target is $\mathbf{x}^* = (0.1, 0.1)$. This target is within the chaotic region displayed in Fig. 12b), close to the unstable manifold of the Duffing equation. It is observed that minimum values are reached on the stable manifold and that the structure of L_{UQ} is correlated to it. This setting is similar to what was observed for the ocean case described in Section 2, in which the observed oil evolution is aligned with the unstable manifold and minimum values of L_{UQ} are found on the

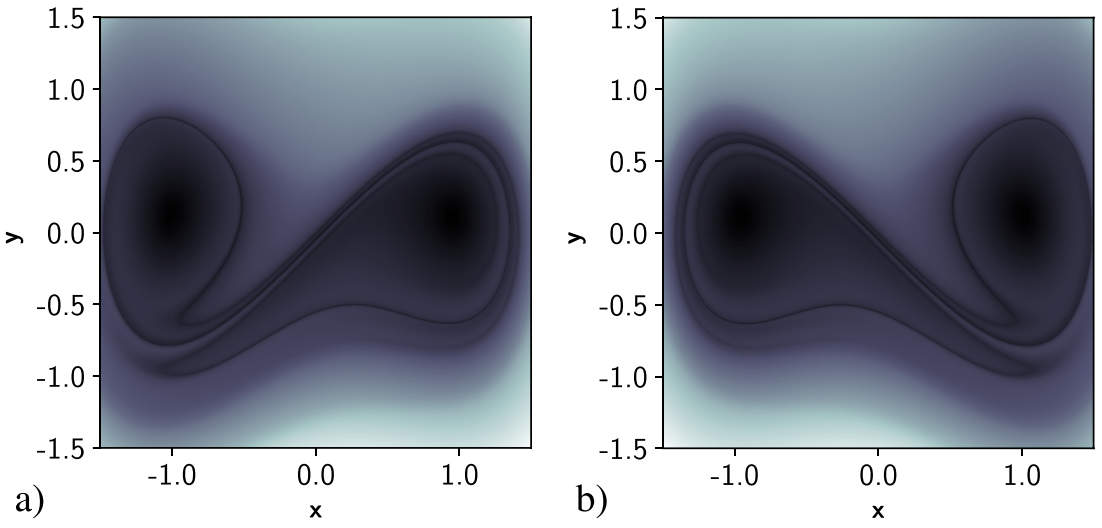

Fig. 13. a) Evaluation of the backwards integration of (6) on the Duffing Eq. (46) at $t_0 = 0$ and $\tau = 10$. This represents the unstable manifold; b) Evaluation of the forwards integration of (6) on the Duffing Eq. (46) at $t_0 = 0$ and $\tau = 10$. This represents the stable manifold.

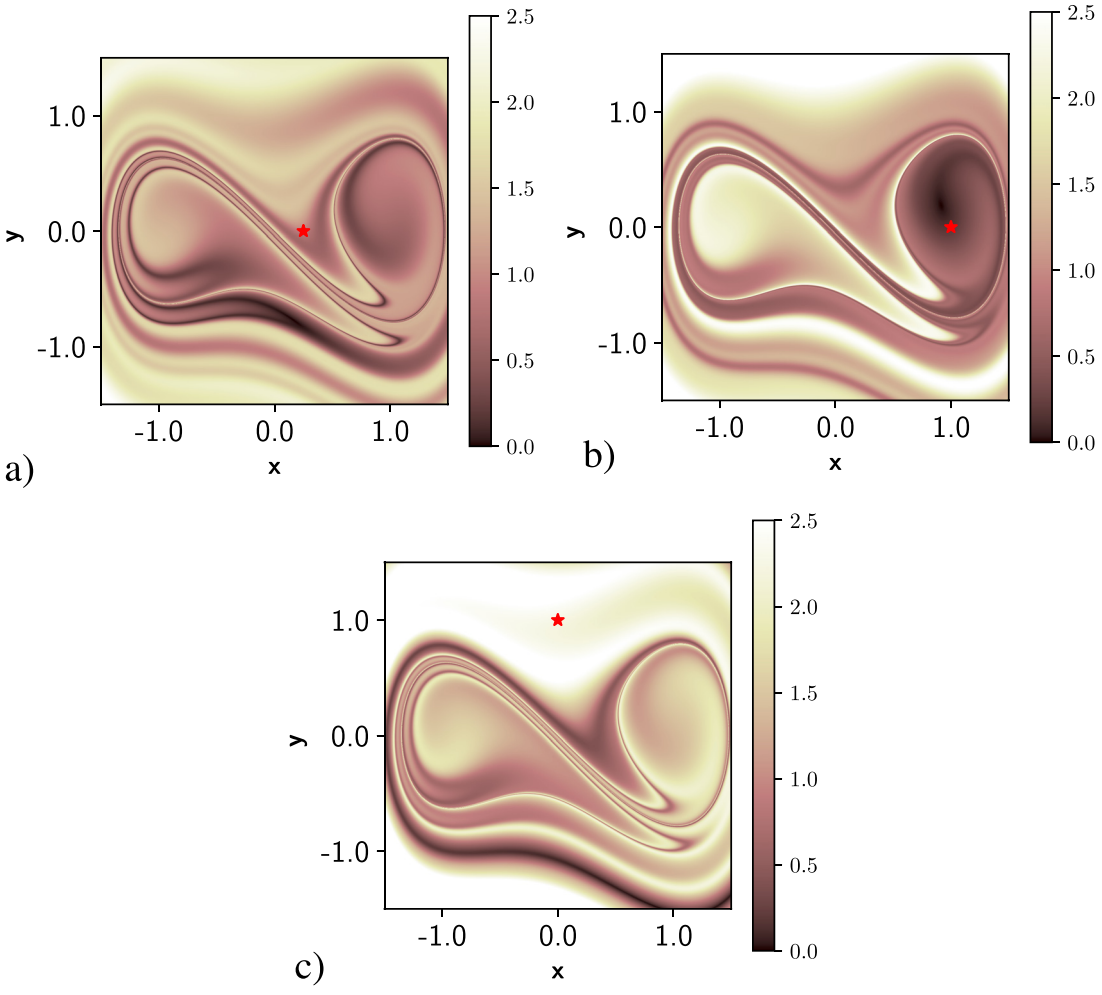

Fig. 14. Evaluation of Eq. (8) on the Duffing Eq. (46) at $t_0 = 0, t = t_0 + \tau = 10$ with different targets. a) Target $\mathbf{x}^* = (0.1, 0.1)$; b) target $\mathbf{x}^* = (1, 0)$; c) target $\mathbf{x}^* = (0, 1)$.

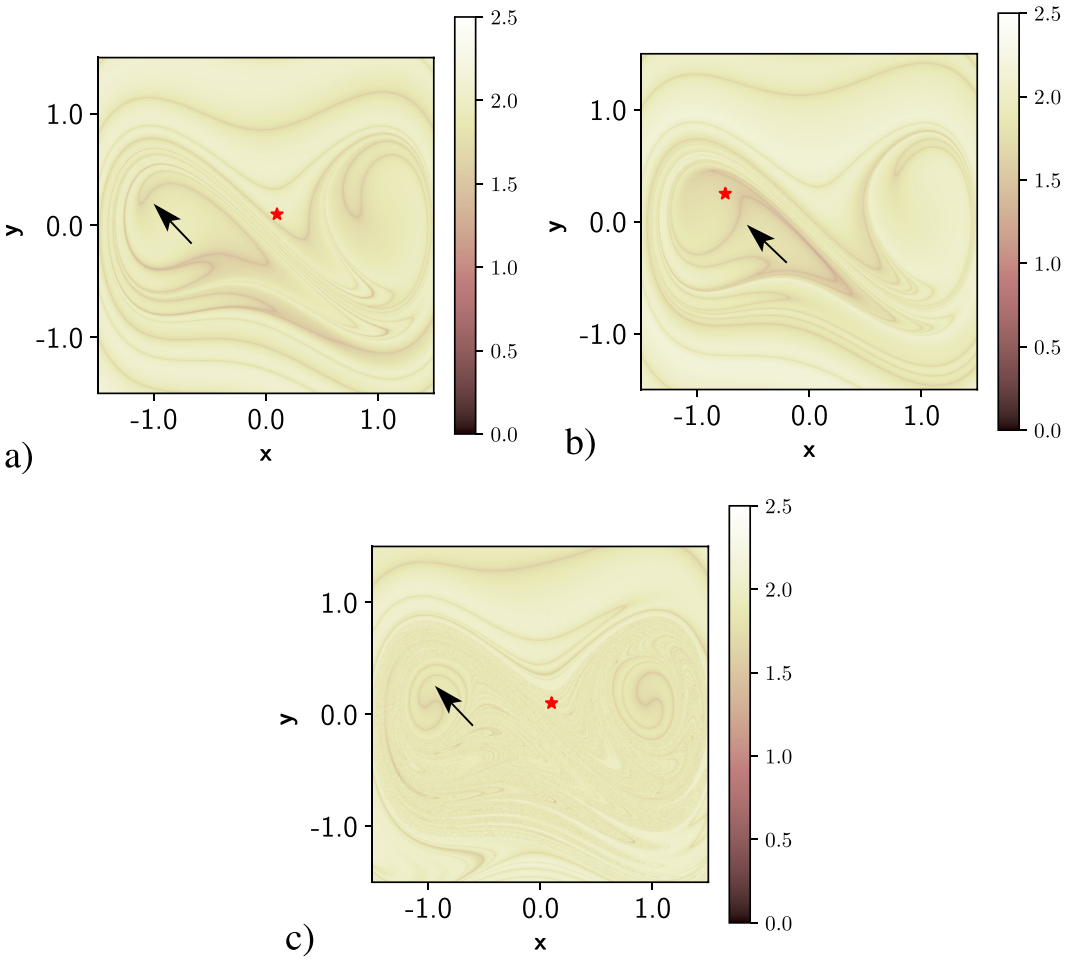

Fig. 15. Evaluation of Eq. (9) on the Duffing Eq. (46) at $t_0 = 0$, for $p = 0.1$ and different targets. Black arrows highlight features that for this system are known to be spurious. a) $t_0 = 0, t = t_0 + \tau = 10$ and target $\mathbf{x}^* = (0.1, 0.1)$; b) $t_0 = 0, t = t_0 + \tau = 10$ and target $\mathbf{x}^* = (-0.75, 0.25)$; c) $t_0 = 0, t = t_0 + \tau = 50$ and target $\mathbf{x}^* = (0.1, 0.1)$

stable manifold that are optimal pathways towards the unstable manifolds. In panel b) we show the results for the target $\mathbf{x}^* = (1, 0)$ which is within the right tori like structure highlighted in Fig. 12b). Accordingly, uncertainty values are very low for initial observations (x_0, y_0) in the corresponding tori region, but very high for the tori like region at the left side. Indeed initial observations in this region will never go near a final observation in the right tori like structure, and therefore this model is *structurally uncertain* for those observations, i.e. the model is inadequate to represent those. Panel c) shows the computation of the uncertainty for a target $\mathbf{x}^* = (0, 1)$ outside the geometry of the unstable invariant manifold displayed in Fig. 13a). It is remarkable the persistence in all these examples of an structure on the uncertainty field with singular features linked to the stable manifold independently of the target value $\mathbf{x}^*$.

Fig. 15 shows the evaluation of Eq. (9) with $p = 0.1$, and different targets or integration periods. Panels a) and b) have the same integration periods, but different targets. In them the black arrow points out different features that seem singular but *do not correspond to any invariant manifold* and in this sense they are spurious. This finding suggests that care must be taken in the invariant interpretation of singular features of Eqs. (8) and (9), although these features truly represent the structure of uncertainty and in this sense they are not spurious. In the next section we will present results in the literature that have used an equation similar to (8) to highlight Lagrangian structures. Fig. 15 c) shows the same than panel a) for an integration period of 50. The black arrow marks a region, which from the analysis of Fig. 12, is known to be covered by tori, while the structure attained from Eq. (9) does not highlight this, again showing the presence of patterns that do not have an invariant interpretation. Indeed, the ergodic partition theory discussed in Mezic and Wiggins [20], Susuki and Mezic [21] and implemented in Lopesino et al. [10] for Lagrangian Descriptors such as that in Eq. (6), shows that this ability to highlight tori, requires averaging along trajectories, while expressions Eq. (8) and (9) *are not averages*, and therefore do

not qualify for the application of ergodic principles. These expressions are not suitable for identifying this kind of invariant objects.

5. Discussion

Our formal results have shown that expressions for uncertainty quantification given in Eqs. (8) and (9) provide singular features associated to the stable invariant manifolds of a hyperbolic trajectory. The numerical evidence found in the realistic ocean application that has motivated the current work indicates that more complex flows in which more hyperbolic trajectories are present will behave the same for each hyperbolic trajectory. The fact that L_{UQ} possess a structure associated with stable invariant manifolds, indicates that in time dependent flows its structure will become more and more complex in longer time intervals, as does the structure of stable manifolds [9,11]. This reveals new hints about the behaviour of uncertainty measurements in long time intervals, which are missed by measures of uncertainty just focused on averages or statistical moments of distributions. However, these statistical measurements are still of much interest to quantify with just one representative number the performance of a data set in a specific application. For instance, if the average of L_{UQ} is considered to be a representative number for uncertainty, the associated uncertainty for the model discussed in the introduction for Figs. 3a), b) and 4 a) is respectively, 0.033°, 0.031° or 0.030°. A comparison of this number for different models allows for determining which one is the most appropriate for describing a particular observation (see [3]).

Recently there has been much interest in uncertainty quantification involving trajectories in ocean data sets. Efforts in this direction are [22–25]. Vieira et al. [25] have developed a clustering method to partition the space of trajectory data sets into distinct flow regions. This method contains free parameters and they use uncertainty quantification to assess the parameter dependence on the partitions they obtain. The work [24] discusses approaches for uncertainty quantification from a geometrical perspective, and uncertainty quantifiers based on distances are proposed, but no connections are proposed with invariant dynamical structures. Similarly in Huntley et al. [23] uncertainty quantifiers based on a descriptive statistics of distances between modelled trajectories and observations are used, but no relations are presented between these and the invariant dynamical structures. Results appeared in Kaszás and Haller [26] also discuss along these lines, but in the context of general models, not related to ocean data. In this work authors have established links between their measure of uncertainty, model sensitivity, and the FTLE field, which is related to invariant manifolds. Authors achieve these results under explicit mathematical assumptions for the "true" model, however results in our work do not require such assumptions for the "ground truth". The FTLE field is constructed from derivatives along trajectories (the Cauchy–Green strain tensor), while the L_{UQ} field is not. It would be an interesting research direction to establish links between the FTLE and the L_{UQ} fields, but the authors have not pursued this.

Equations similar to (8) or (9) have been used in the literature to highlight Lagrangian structures in oceanic flows. For instance [27,28] have done so. Prants et al. [27] proposed to use the arc-length D to study the displacement of particles in the coasts of Japan.

$$D = \sqrt{(x_f - x_0)^2 + (y_f - y_0)^2}. \tag{47}$$

Here, D represents the relative displacement of a particle from its initial position (x_0, y_0) to certain final one (x_f, y_f). This expression is the analogue to Eq. (8) with $p = 2$ and target adjusted to each initial condition. However, in this work no connections are established between Eq. (47) and uncertainty quantification. On the other hand, our results in the previous section indicate that nonlinearities introduce features in the L_{UQ} pattern that do not have an invariant interpretation.

6. Conclusions

This article explores a definition for Uncertainty Quantification recently proposed in oceanic contexts [3]. The findings described in this article are of particular interest for they have important environmental applications. Nowadays, multiple ocean data sources are available and in this context our results allow a quantitative comparison of the transport properties associated with them. In this way discriminating the level of performance of different data sources will help to gain precision in the description of dispersion of contaminants, determination of waste and plastic sources, etc.

We have also examined the implications of this definition. It is found that for this definition, which is associated to forward Uncertainty Quantification, stable invariant manifolds of hyperbolic trajectories of the underlying flow, provide a structure for it. That is, we found that the proposed Uncertainty Quantifier is a function that contains a very rich structure, particularly for long time intervals, which is related to these well known structures from dynamical systems theory. For selected examples this statement has been proven. Also examples are discussed in which singular structures of the Uncertainty Quantifier highlights structures that are not aligned with invariant features of the dynamical system. Other invariant structures like tori, are not recovered by the Uncertainty Quantifier. Also, connections between UQ and invariant dynamical structures have been used to provide a framework for discussion on structural uncertainty, which is related to inadequate models. This vision enriches traditional descriptions of UQ on which structure is discussed just in terms of means and/or statistical moments of distributions.

Declaration of Competing Interest

The authors declare that they have no known competing financial interests or personal relationships that could have appeared to influence the work reported in this paper.

CRediT authorship contribution statement

G. García-Sánchez: Conceptualization, Software, Investigation, Data curation, Visualization. **A.M. Mancho:** Conceptualization, Software, Supervision, Validation, Methodology, Writing – original draft. **S. Wiggins:** Conceptualization, Supervision, Validation, Writing – review & editing.

Acknowledgements

GGS and AMM acknowledge support from IMPRESSIVE, a project funded by the European Union's Horizon 2020 research and innovation programme under grant agreement no. 821922. SW acknowledges the support of ONR Grant no. N00014-01-1-0769 and EPSRC Grant no. EP/P021123/1. We acknowledge the use of ICMAT computational facilities. The authors acknowledge support of the publication fee by the CSIC Open Access Publication agreement with Elsevier.

References

[1] Frenklach M, Packard A, Garcia-Donato G, Paulo R, Sacks J. Comparison of statistical and deterministic frameworks of uncertainty quantification. SIAM/ASA J Uncertain Quantif 2016;4(1):875–901.
[2] Sullivan TJ. Introduction to uncertainty quantification. Springer; 2015.
[3] García-Sánchez G, Mancho AM, Ramos AG, Coca J, Pérez-Gómez B, Álvarez-Fanjul E, Sotillo MG, García-León M, García-Garrido VJ, Wiggins S. Very high resolution tools for the monitoring and assessment of environmental hazards in coastal areas. Front Mar Sci 2021;7:605804.
[4] Sotillo MG, Cerralbo P, Lorente P, Grifoll M, Espino M, Sanchez-Arcilla A, Álvarez-Fanjul E. Coastal ocean forecasting in Spanish ports: the SAMOA operational service. J Oper Oceanogr 2020;13(1):37–54.
[5] Palis J. On Morse–Smale dynamical systems. Topology 1968;8:385–404.
[6] de Melo W, Palis J. Geometric theory of dynamical systems: an introduction. New York: Springer-Verlag; 1982.
[7] Madrid JAJ, Mancho AM. Distinguished trajectories in time dependent vector fields. Chaos 2009;19:013111.
[8] Mendoza C, Mancho AM. The hidden geometry of ocean flows. Phys Rev Lett 2010;105(3):038501.
[9] Mancho AM, Wiggins S, Curbelo J, Mendoza C. Lagrangian descriptors: a method for revealing phase space structures of general time dependent dynamical systems. Commun Nonlinear Sci Numer 2013;18:3530–57.
[10] Lopesino C, Balibrea-Iniesta F, García-Garrido VJ, Wiggins S, Mancho AM. A theoretical framework for Lagrangian descriptors. Int J Bifurc Chaos 2017;27(01):1730001.
[11] Mendoza C, Mancho AM. The hidden geometry of ocean flows. Phys Rev Lett 2010;105(3):038501.
[12] Mendoza C, Mancho AM. The Lagrangian description of aperiodic flows: a case study of the Kuroshio current. Nonlinear Process Geophys 2012;19(4):449–72.
[13] de la Cámara A, Mechoso CR, Serrano E, Ide K. Quasi-horizontal transport within the Antarctic polar night vortex: Rossby wave breaking evidence and Lagrangian structures. J Atmos Sci 2013;70:2982–3001.
[14] Mancho AM, Small D, Wiggins S, Ide K. Computation of stable and unstable manifolds of hyperbolic trajectories in two-dimensional, aperiodically time-dependent vectors fields. Phys D 2003;182:188–222.
[15] Mancho AM, Small D, Wiggins S. A tutorial on dynamical systems concepts applied to Lagrangian transport in oceanic flows defined as finite time data sets: theoretical and computational issues. Phys Rep 2006;437:55–124.
[16] Mancho AM, Small D, Wiggins S. Computation of hyperbolic and their stable and unstable manifolds for oceanographic flows represented as data sets. Nonlinear Process Geophys 2004;11:17–33.
[17] Lopesino C, Balibrea F, Wiggins S, Mancho AM. Lagrangian descriptors for two dimensional, area preserving, autonomous and nonautonomous maps. Commun Nonlinear Sci Numer Simul 2015;27(1-3):40–51.
[18] García-Garrido VJ, Balibrea-Iniesta F, Wiggins S, Mancho AM, Lopesino C. Detection of phase space structures of the cat map with Lagrangian descriptors. Regul Chaotic Dyn 2018;23(6):751–66.
[19] Moser J. The analytic invariants of an area-preserving mapping near a hyperbolic fixed point. Commun Pure Appl Math 1956;9:673–92.
[20] Mezic I, Wiggins S. A method for visualization of invariant sets of dynamical systems based on the ergodic partition. Chaos 1999;9:213–18.
[21] Susuki Y, Mezic I. Ergodic partition of phase space in continuous dynamical systems. Proceedings of the Joint 48th IEEE Conference on Decision and Control and 28th Chinese Control Conference (CDC/CCC2009) (2009): 7497–7502.
[22] Kirwan AD Jr, Toner M, Kantha L. Predictability, uncertainty, and hyperbolicity in the ocean. Int J Eng Sci 2003;41:249.
[23] Huntley SH, Lipphardt BL Jr, Kirwan AD Jr. Lagrangian predictability assessed in the east china sea. Ocean Model 2011;36:163.
[24] Feng D, Passalacqua P, Hodges BR. Innovative approaches for geometric uncertainty quantification in an operational oil spill modeling system. J Mar Sci Eng 2019;7(8):259.
[25] Vieira GS, Rypina II, Allshouse MR. Uncertainty quantification of trajectory clustering applied to ocean ensemble forecasts. Fluids 2020;5(4):184.
[26] Kaszás B, Haller G. Universal upper estimate for prediction errors under moderate model uncertainty. Chaos 2020;30:113144.
[27] Prants S, Uleysky MY, Budyansky M. Numerical simulation of propagation of radioactive pollution in the ocean from the Fukushima Dai-ichi nuclear power plant. In: Doklady earth sciences, 439. Springer; 2011. p. 1179.
[28] Prants S, Budyansky M, Uleysky MY. Lagrangian study of surface transport in the Kuroshio extension area based on simulation of propagation of Fukushima-derived radionuclides. Nonlinear Process Geophys 2014;21(1):279–89.